

## Article

# Zn-Al Ferrite/Polypyrrole Nanocomposites: Structure and Dielectric and Magnetic Properties for Microwave Applications

Huda F. Khalil <sup>1,\*</sup>, Sherif G. Elsharkawy <sup>2</sup>, Nouf F. AL-Harby <sup>3,\*</sup> and Mervette El-Batouti <sup>4</sup>

<sup>1</sup> Electronic Materials Department, Advanced Technology and New Material Institute (ATNMI), City of Scientific Research and Technological Applications (SRTA-City), Alexandria 21934, Egypt

<sup>2</sup> Basic and Applied Sciences, College of Engineering and Technology, AASTMT, Alexandria 21934, Egypt; ssharkawy@aast.edu

<sup>3</sup> Department of Chemistry, College of Science, Qassim University, Buraydah 51452, Saudi Arabia

<sup>4</sup> Chemistry Department, Faculty of Science, Alexandria University, Alexandria 21934, Egypt; mervette\_b@yahoo.com

\* Correspondence: hudafarid85@gmail.com (H.F.K.); hrbien@qu.edu.sa (N.F.A.-H.)

**Abstract:** In this study, Zn-Al ferrite/polypyrrole (PPy) nanocomposites were synthesized and thoroughly characterized to explore their potential for microwave applications. X-ray diffraction analysis confirmed the presence of ZnO, AlFeO<sub>3</sub>, and Fe<sub>2</sub>O<sub>3</sub> phases, with the crystal size decreasing from 31 nm to 19.6 nm as aluminum content increased. High-resolution transmission electron microscopy (HR-TEM) revealed a distinctive core-shell morphology, where the polypyrrole encapsulates the ZnAl<sub>x</sub>Fe<sub>2-x</sub>O<sub>4</sub> particles. Magnetic measurements showed that decreasing aluminum concentration led to a reduction in both saturation magnetization (M<sub>s</sub>) from 75 emu/g to 36 emu/g and remanent magnetization (M<sub>r</sub>) from 2.26 emu/g to 2.00 emu/g. Dielectric analysis indicated that both the real (ε') and imaginary (ε'') components of dielectric permittivity decreased with increasing frequency, particularly between 10 and 14 GHz. Furthermore, electrical modulus analysis highlighted the significant impact of aluminum doping on relaxation time (τIP), indicating the presence of interface polarization. Impedance spectroscopy results underscored the dominance of interface polarization at lower frequencies and the presence of strong conduction paths at higher frequencies. These combined magnetic and dielectric loss mechanisms suggest that the Zn-Al ferrite/polypyrrole nanocomposite is a promising candidate for advanced microwave absorption applications.

**Keywords:** Zn-Al ferrite; polypyrrole; nanocomposites; magnetic properties; dielectric properties; microwave absorption; impedance spectroscopy; core-shell structure



**Citation:** Khalil, H.F.; Elsharkawy, S.G.; AL-Harby, N.F.; El-Batouti, M. Zn-Al Ferrite/Polypyrrole Nanocomposites: Structure and Dielectric and Magnetic Properties for Microwave Applications. *Polymers* **2024**, *16*, 2432. <https://doi.org/10.3390/polym16172432>

Academic Editors: Bing Wang, Chenglong Guan and Lihua Zhan

Received: 5 August 2024

Revised: 21 August 2024

Accepted: 25 August 2024

Published: 28 August 2024



**Copyright:** © 2024 by the authors. Licensee MDPI, Basel, Switzerland. This article is an open access article distributed under the terms and conditions of the Creative Commons Attribution (CC BY) license (<https://creativecommons.org/licenses/by/4.0/>).

## 1. Introduction

Microwave technology has become increasingly important in various applications, including telecommunications, radar systems, and energy transmission. However, the efficiency of microwave energy utilization remains a critical challenge. Many researchers have made efforts to develop advanced microwave-absorbing materials that can be used in the field of microwave applications [1]. Nanocomposites have been raised among these materials, combining different elements for more refined and improved performance. Then, further investigations have been made to include polymers in addition to these nanocomposites, for example, Mn-Zn ferrites [2], Cu-Zn ferrites [3], ZnFe<sub>2</sub>O<sub>4</sub> [4], and Zn<sub>0.5</sub>Ni<sub>0.4</sub>Cr<sub>0.1</sub>Fe<sub>2</sub>O<sub>4</sub> [5], all these nanocomposites are fabricated by combining the ferrite with conductive polymers like polyaniline (PANI) and polypyrrole (PPy). These nanocomposites have shown excellent microwave absorption performance, which is attributed to the effects of magnetic and dielectric losses.

Throughout this work, spinel ferrites, such as zinc-aluminum (Zn-Al) ferrite, have been given significant attention due to their excellent dielectric and magnetic properties, making them suitable for microwave absorption applications [6,7]. Polypyrrole, PPy [8], has

been widely used with various ferrites to increase the magnetization saturation ( $M_s$ ), and their ability to absorb electromagnetic waves makes them suitable for shielding electronic devices from unwanted interference. Accurately mixed ferrite powder with PPy produces nanocomposites characterized by highly dielectric and magnetic properties. Understanding the interplay between the spinel ferrite and conductive polymer components will contribute to the development of advanced microwave-absorbing materials, ultimately leading to improved efficiency and performance in various microwave-based technologies. The improved structure of the Zn-Al ferrite/PPy nanocomposite leads to better electromagnetic interference (EMI) shielding performance [9]. Moreover, this structure constitutes various applications, including radar stealth technology, wireless communication systems, and electromagnetic compatibility. In this work, the microwave absorption properties of the Zn-Al ferrite/PPy nanocomposite will be explored, and the potential for effective microwave absorption and shielding in diverse microwave-based applications will be discussed. This will be achieved by investigating the structural, dielectric, and magnetic properties of Zn-Al ferrite/PPy nanocomposites, with the goal of advancing the efficiency of microwave applications. The research will focus on the synthesis, characterization, and evaluation of the nanocomposites' performance, providing insights into the underlying mechanisms responsible for their enhanced microwave absorption capabilities.

## 2. Experimental Techniques and Procedures

ZnAl<sub>x</sub>Fe<sub>2-x</sub>O<sub>4</sub>/polypyrrole nanocomposite with concentrations of  $x$  (wt.%) = 0.0, 0.2, 0.4, 0.6, and 0.8 were synthesized using solid-state reaction technique [8]. The zinc oxide (ZnO), aluminum oxide (Al<sub>2</sub>O<sub>3</sub>), iron oxide (Fe<sub>2</sub>O<sub>3</sub>), and polypyrrole (PPy) powders were weighed according to the desired composition ratio (wt.%) for each sample. ZnO, Al<sub>2</sub>O<sub>3</sub>, and Fe<sub>2</sub>O<sub>3</sub> powders were obtained from Sigma-Aldrich; also, PPy was synthesized using a chemical polymerization method. A calculated amount of PPy powder, approximately 30% of the total weight of the nanocomposite, was added to the weighed ZnO, Al<sub>2</sub>O<sub>3</sub>, and Fe<sub>2</sub>O<sub>3</sub> powders. Then, the mixture was further ground to evenly distribute the PPy within the ZnAl<sub>x</sub>Fe<sub>2-x</sub>O<sub>4</sub> matrix with ball milling. Finally, the mixture was calcinated at 850° for 7 h. After the calcination process, the resultant nanocomposite powder was removed from the furnace and allowed to cool down to room temperature. The synthesized ZnAl<sub>x</sub>Fe<sub>2-x</sub>O<sub>4</sub>/PPy nanocomposite was characterized using X-ray diffraction (XRD) using X'Pert Philips (Eindhoven, The Netherlands) powder diffractometer with CuK $\alpha$  radiation ( $\lambda = 1.54056 \text{ \AA}$ ) in the range  $10^\circ \leq 2\theta \leq 80^\circ$ . Additionally, the morphology of the specimens was investigated using High-Resolution Transmission Electron Microscopy (TEM), JEOL-JEM-2100 (Tokyo, Japan) equipment was operated at 200 kV, and included a SAED (Selected Area Electron Diffraction) mode. The magnetic hysteresis loops were measured at room temperature using a vibrating sample magnetometer (VSM) operating system 7400 Series-Lake Shore Cryotronics (Westerville, OH, USA). The frequency-dependent electromagnetic properties and microwave shielding measurements were carried out on a vector network analyzer (model 8510–45 MHz to 26.56 GHz, USA) by waveguide transmission line technique. A vector network analyzer (VNA) for the microwave measurements was used. The measurements were carried out using the free space method, which is ideal for minimizing interference from external sources and ensuring accurate results. The configuration involved positioning the sample between two horn antennas in a free-space environment to measure the S-parameters (S<sub>11</sub> and S<sub>21</sub>). The S-parameters were then used to extract the complex permittivity ( $\epsilon$ ) and permeability ( $\mu$ ) of the material. The extraction was performed using the Nicolson–Ross–Weir (NRW) method, a well-established technique for determining electromagnetic properties from S-parameter measurements. All instruments and methodologies used in this study were carefully selected to ensure high precision and reliability of the results.

### 3. Results and Discussion

#### 3.1. XRD Analysis

The XRD peaks of  $\text{ZnAl}_x\text{Fe}_{2-x}\text{O}_4$ /polypyrrole nanocomposites with concentrations of  $x$  (wt.%) = 0.0, 0.2, 0.4, 0.6, and 0.8 are shown in Figure 1a. The XRD of the nanocomposite with  $x = 0.0$  (wt.%) showed strong diffraction at  $2\theta = 31.82^\circ, 34.21^\circ, 36.33^\circ, 47.49^\circ, 56.52^\circ, 62.90^\circ, 67.95^\circ, 69.01^\circ,$  and  $78.32^\circ$ , corresponding to 100, 002, 200, 102, 125, 103, 112, 201, and 202 planes, respectively. The nanocomposite structure of Zn-Al ferrite/PPy contains three phases: the ZnO hexagonal phase (JCPDS No: 01-079-2205),  $\text{AlFeO}_3$  orthorhombic phase (JCPDS No: 01-084-2153), and  $\text{Fe}_2\text{O}_3$  rhombohedral phase (JCPDS No. 01-084-0308). Figure 1b illustrates the crystallite size ( $D$ ) nm, and Figure 1c shows the lattice microstrain ( $\varepsilon$ ) and dislocation density ( $\delta$ ) $\text{nm}^{-3}$  for  $\text{ZnAl}_x\text{Fe}_{2-x}\text{O}_4$ /polypyrrole nanocomposites with concentrations of  $x$  (wt.%) = 0.0, 0.2, 0.4, 0.6, and 0.8. The corresponding results are tabulated below in Table 1 and were obtained using the following formulae [10,11]:

$$D = \frac{k\lambda}{\beta \cos\theta} \quad (1)$$

$$\varepsilon = \frac{\beta \cos\theta}{4} \quad (2)$$

$$\delta = \frac{1}{D^2} \quad (3)$$

where ( $k$ ) is the Scherer's constant, typically taken as 0.89; ( $\lambda$ ) is the wavelength of the X-rays; ( $\beta$ ) is the full width at half-maximum (FWHM) of the diffraction peak; and  $\theta$  is the Bragg's angle. From Figure 1b, the crystallite size,  $D$ , was observed to decrease from 30.01 to 19.89 nm as the  $\text{Al}^{3+}$  substitution ratios  $x$  (wt.%) were increased from 0.0 to 0.8, showing a 66.27% loss in the total crystallite size. This reduction in size could be referenced to the disruption of the crystal growth process due to the differing atomic size, bonding, and diffusion characteristics of the substituted  $\text{Al}^{3+}$  ions compared to the original  $\text{Fe}^{3+}$  ions. The inhibition of the diffusion of atoms necessary for continued crystal growth is caused by the altered atomic interactions and mobility introduced by the  $\text{Al}^{3+}$  substitution. Moreover, the crystal structure destabilizes and hinders long-range crystal order due to the incorporation of smaller  $\text{Al}^{3+}$  ions. The increased lattice strain and defects introduced by the size mismatch between the substituted  $\text{Al}^{3+}$  and original  $\text{Fe}^{3+}$  ions interrupts the normal crystal nucleation and growth mechanisms. The presence of the  $\text{Al}^{3+}$  ions disrupts the regular crystal formation processes [12,13]. Doping can alter the nucleation and growth kinetics of crystallites, leading to variations in size. Conversely, the lattice microstrain and dislocation density exhibited an opposing trend, as illustrated in Figure 1c. Certainly, the opposing trend observed suggests an intriguing aspect of the material's behavior. This can be attributed to the introduction of  $\text{Al}^{3+}$  as a dopant; the incorporation of foreign atoms into the crystal lattice may cause lattice distortion or mismatches, contributing to an increase in lattice strain [14,15].

**Table 1.** Crystalline size,  $D$  (nm); microstrain,  $\varepsilon$ ; and dislocation,  $\delta$  ( $\text{nm}^{-3}$ ).

$x$ (wt.%)	$D$ (nm)	$\varepsilon$	$\delta$ ( $\text{nm}^{-3}$ )
0.0	30.01	0.00072	0.00111
0.2	27.13	0.00107	0.00136
0.4	23.90	0.00135	0.00175
0.6	21.02	0.00169	0.00226
0.8	19.89	0.00175	0.00253

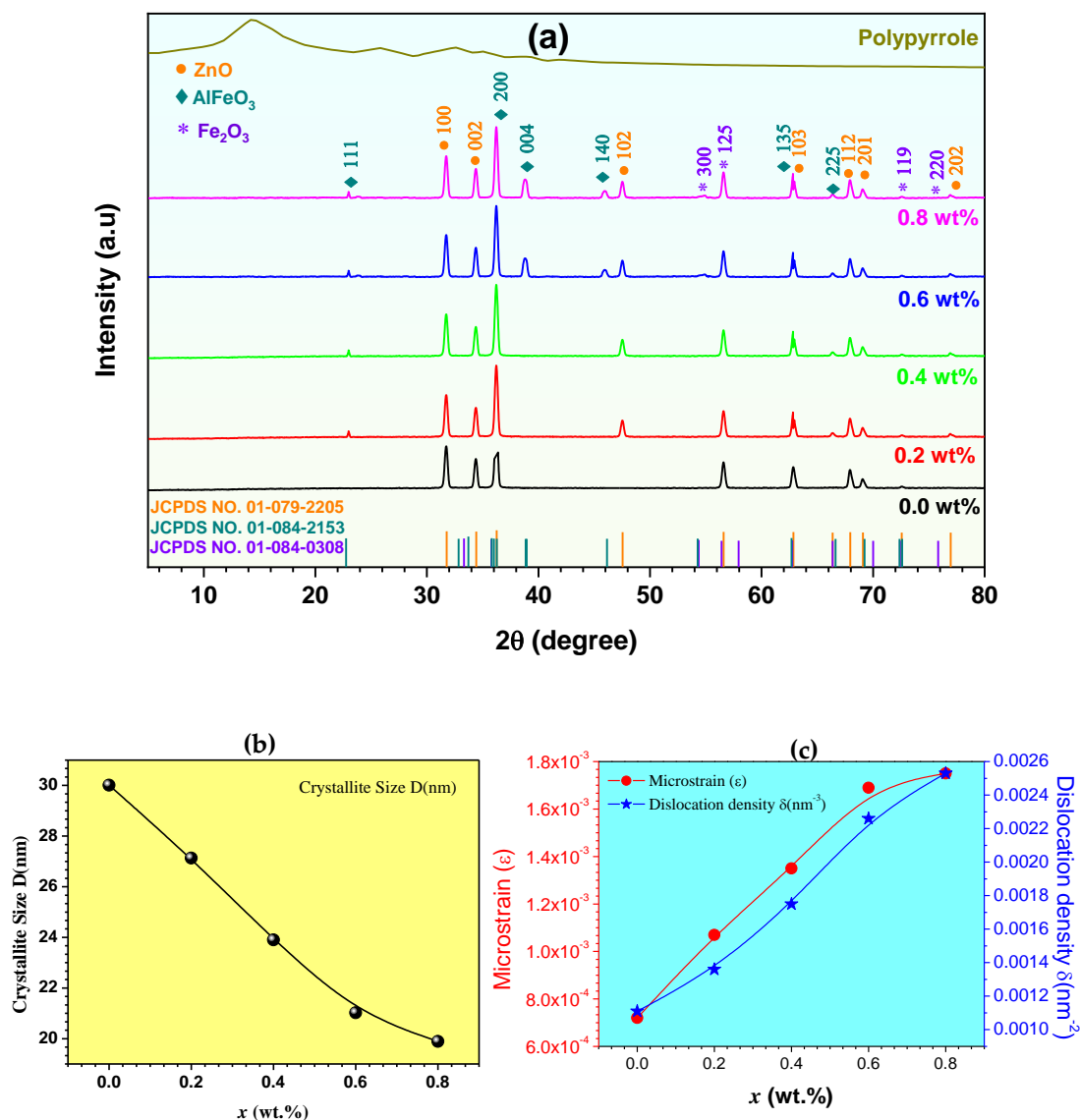


**Figure 1.** (a) XRD of  $\text{ZnAl}_x\text{Fe}_{2-x}\text{O}_4$ /polypyrrole nanocomposite with concentrations of  $x$  (wt.%) = (0.0, 0.2, 0.4, 0.6, and 0.8). (b) crystallite size  $D$  (nm), (c) microstrain ( $\epsilon$ ), and dislocation density  $\delta$  ( $\text{nm}^{-3}$ ) of the nanocomposite.

### 3.2. Morphology

The morphology of the  $\text{ZnAl}_x\text{Fe}_{2-x}\text{O}_4$ /polypyrrole composite powders was characterized using transmission electron microscopy (TEM), as shown in Figure 2a–e. For each compound, a TEM image (100 nm scale), an HR-TEM image (10 nm scale) (see Figure 2a'–e'), another HR-TEM image (1 nm scale) (see Figure 2a''–e''), and a SAED diagram (see Figure 2A–E) are presented. TEM patterns show a significant difference in particle shape upon the substitution of Zn for Al in the spinel framework. Figure 2a,d show that most of the  $\text{ZnAl}_x\text{Fe}_{2-x}\text{O}_4$  particles at concentrations of  $x = 0.0$  and 0.6 are faceted with a hexagonal shape [16]. These nanoparticles adopted a well-defined polyhedral morphology with an alignment of 100 nm. This implies that the high calcination temperature (850 °C) not only affects the shape but also the size of the particles. However, in Figure 2e, primary particles have irregular shapes and are agglomerated, a morphology inside the composite. This indicates that the coexistence of the  $\text{ZnAl}_x\text{Fe}_{2-x}\text{O}_4$  spinel and the secondary  $\text{Fe}_2\text{O}_3$  phase results in a polycrystalline sample with a large proportion of irregularly shaped particles, where HR-TEM Figure 2b'',d'' enlarged from the selected area show lattice fringes

with interplanar distances of 0.307, 0.339, and 0.348 nm for  $\text{ZnAl}_{0.2}\text{Fe}_{1.8}\text{O}_4$ ,  $\text{ZnAl}_{0.4}\text{Fe}_{1.6}\text{O}_4$ , and  $\text{ZnAl}_{0.6}\text{Fe}_{1.4}\text{O}_4$  samples, respectively. These match well with the (111) plane of the  $\text{Fd}3\text{m}$  spinel phase. A careful examination of the HR-TEM of Zn-rich  $\text{ZnAl}_{0.8}\text{Fe}_{1.2}\text{O}_4$  in Figure 2e exposes the presence of a matrix corresponding to the  $\text{Fe}_2\text{O}_3$  and  $\text{Al}_2\text{O}_3$  phases. The SAED patterns in Figure 2A–E provide important insights into the crystal structures; where  $x = 0.0$  wt.%, the diffraction spots are indicative of a well-defined crystalline structure. The rings in the pattern correspond to specific planes of the spinel structure. In Figure 2B, for the  $\text{ZnAl}_{0.2}\text{Fe}_{1.8}\text{O}_4$ /polypyrrole composite, the diffraction spots are slightly less sharp than in Figure 2A, indicating a minor structural disorder. For Figure 2C–E, the SAED pattern shows more pronounced rings, suggesting an increase in structural disorder. The presence of rings alongside spots indicates that the samples contain regions of crystallinity as well as areas with less order, possibly due to the presence of secondary phases.

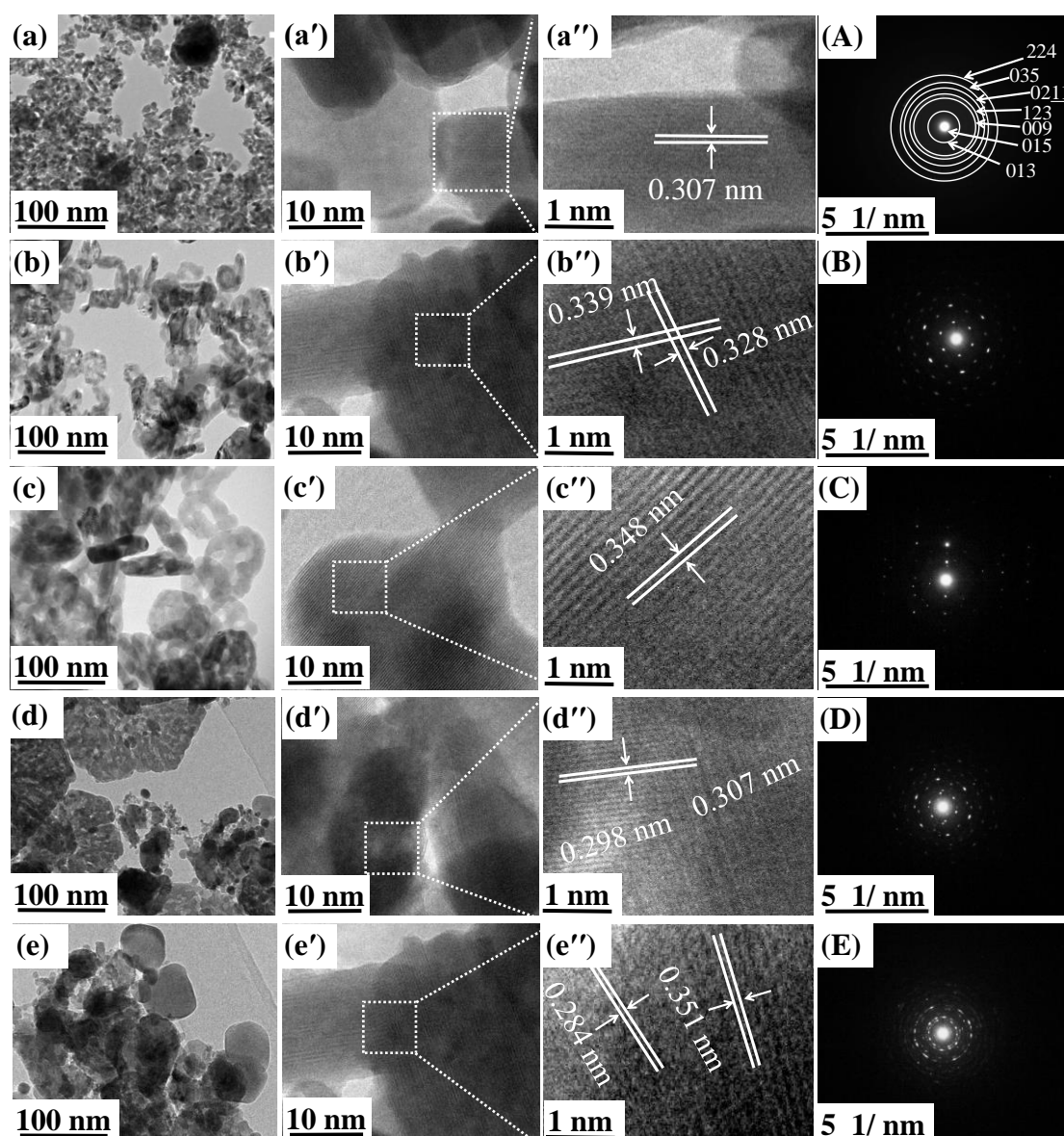


**Figure 2.** HR-TEM images of  $\text{ZnAl}_x\text{Fe}_{2-x}\text{O}_4$ /polypyrrole nanocomposite with concentrations of  $x$  (wt.%) = 0.0, 0.2, 0.4, 0.6, and 0.8, (a–e) alignment 100 nm, (a'–e') alignment 10 nm, (a''–e'') alignment 1 nm, and (A–E) SEAD.

### 3.3. Magnetic Properties

Figure 3 shows the magnetic hysteresis loop for the  $\text{ZnAl}_x\text{Fe}_{2-x}\text{O}_4$ /polypyrrole nanocomposite, with key magnetic properties at ambient temperature, such as loop area, saturation magnetization ( $M_s$ ), remanence magnetization ( $M_r$ ), the ratio of  $M_r$  to  $M_s$  (squareness), and coercivity ( $H_c$ ), presented in Table 2. Given the polycrystalline nature of the structure with a size under 10 nm, it is likely to possess a mono-domain configuration, facilitating alignment with the external magnetic field with relative ease [17]. A notably low coercivity of 124.53 KOe suggests minimal resistance to domain alignment, with the unsaturated magnetization further implying a singular domain structure. The minimum value of  $M_r/M_s$  composites superparamagnetic-like properties. Polypyrrole, within this context, acts as a barrier to domain alignment under an external magnetic field but facilitates domain rotation when the field's strength increases. The composite film's squareness value, standing at a mere 0.106, reflects its soft magnetic ferrite nature [18]. The incorporation of polypyrrole, particularly at an  $x$  value of 0.6, degrades the magnetic attributes of the composites, leading to decreased saturation and remanence magnetizations. Specifically, the  $M_s$  and  $M_r$  readings for  $x = 0.6$  are markedly reduced, registering at 0.4575 emu/g and  $48.75 \times 10^{-3}$  emu/g, respectively, an effect attributed to the diminished A-B exchange interaction caused by polypyrrole.

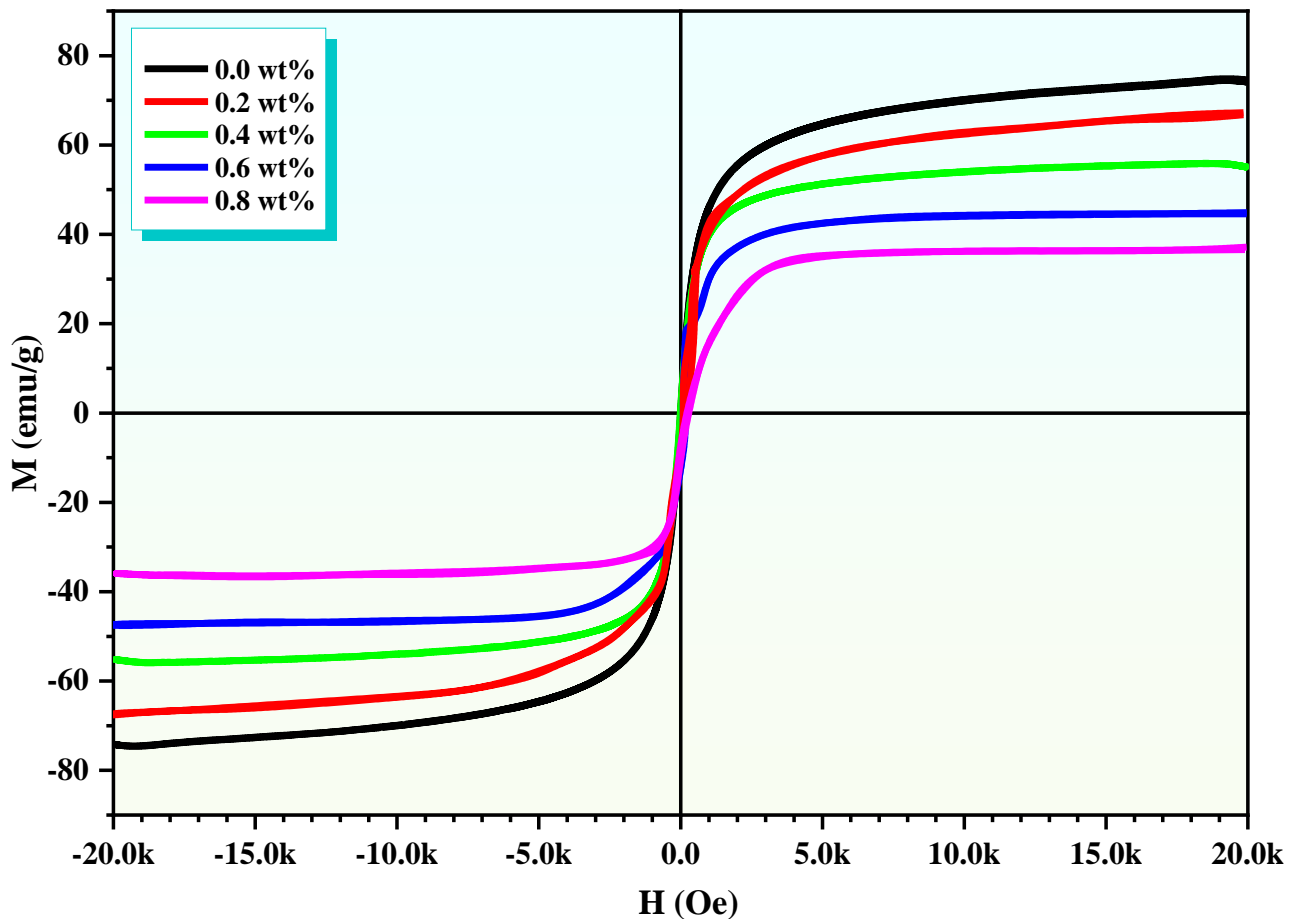


**Figure 3.** The hysteresis loops for  $\text{ZnAl}_x\text{Fe}_{2-x}\text{O}_4$ /polypyrrole nanocomposite at  $x = 0.0, 0.2, 0.4, 0.6,$  and  $0.8$  wt.%.

**Table 2.** Saturation magnetization (Ms), remanent magnetization (Mr), coercivity (Hc), (Mr/Ms), and magnetic moment ( $\mu\text{B}$ ) of  $\text{ZnAl}_x\text{Fe}_{2-x}\text{O}_4$ /polypyrrole nanocomposite with concentrations of  $x$  (wt.%) = 0.0, 0.2, 0.4, 0.6, and 0.8.

$x$ (wt.%)	Ms (emu/g)	Mr (emu/g)	Hc (Oe)	Mr/Ms	$\mu\text{B}$
0.0	75	2.26	38.91	0.030	10.79
0.2	67	3.87	38.52	0.057	9.17
0.4	55	2.19	38.86	0.039	7.15
0.6	45	1.48	39.17	0.032	5.54
0.8	36	2.00	39.64	0.055	4.18

#### 4. Dielectric and Microwave Properties

The dielectric properties of the composite depend on the frequency subjected, which is closely linked to the polarizability and orientation of the present dipoles. As the frequency of the applied field increases, the dipoles of the system struggle to match the changing field faster, giving decline to the real and imaginary parts of the dielectric constant ( $\epsilon'$ ) and ( $\epsilon''$ ), respectively. The value of  $\epsilon'$  represents the strength of the dielectric polarization, which indicates the ability of the material to store electricity, while  $\epsilon''$  indicates the energy transfer to the dielectric material [19]. These values vary with the dielectric loss tangent ( $\tan \delta = \epsilon'' / \epsilon'$ ) at different frequencies. The frequency-dependent dielectric response of polypyrrole/Zn-Al ferrite nanocomposites with different Al content, as shown in Figure 4, was measured at ambient temperature in the frequency range of 10–17 GHz. The observation of a dielectric diffusion pattern shows a significant decrease in the values of  $\epsilon'$  and  $\epsilon''$ , especially in the range of 10–15 GHz [20]. From this point on,  $\epsilon'$  decreases linearly up to 17 GHz, while  $\epsilon''$  and  $\tan \delta$  remain constant, unaffected by frequency changes. The initial phase decreases  $\epsilon'$  and  $\epsilon''$  are mainly due to the frequency elevation affecting the interface polarization, which is caused by charge accumulation at the interfaces between the conducting and dielectric blocks under an alternating electric field. Moreover, charge hopping plays an important role in Zn-Al ferrite. Nanostructures, with a large surface area compared to their size, exhibit numerous defects, dipoles, and unpaired bonds, enhancing the dipolar electron polarization effect and thus enhancing interface polarization. Generally, Zn-Al ferrite nanoparticles exhibit higher  $\epsilon'$ ,  $\epsilon''$ , and  $\tan \delta$  values compared to polypyrrole/Zn-Al ferrite nanocomposites.  $\text{ZnAl}_x\text{Fe}_{2-x}\text{O}_4$ /polypyrrole composites, characterized by a dense granular structure coated with polypyrrole chains on ferrite particles, exhibit variable electrical properties due to interactions between ferrite and polypyrrole to initiate polymerization, which can be degraded polymer chains and block electrical conductivity [21]. The encapsulation of ferrite nanoparticles in polypyrrole lowers the electron density, resulting in decreased conductivity. The addition of ZnAl ferrite to the polypyrrole matrix creates an additional space charge at the interface. Increasing the amount of Al increases the number of free valence electrons, which affects the conductivity properties of the composite. Figure 4c,d presents the frequency-dependent behavior of the electric modulus components,  $\mu'$  and  $\mu''$ , along with their representation on a Cole–Cole plot ( $M'$  versus  $M''$ ). The  $M'$  component showcases a progressive increase up to a frequency of  $f = 17$  GHz, with enhanced values for the sample enriched with a higher Al concentration. Notably, at lower frequencies, the  $M'$  values are non-zero, suggesting that the diminished  $\epsilon'$  values in these samples are not influenced by electrode polarization (EP) effects. There's a clear correlation observed between the rising  $M'$  values and the decreasing  $\epsilon'$  values. Space charge accumulation within electrical insulation emerges as a significant issue, as it amplifies the internal electric fields, potentially leading to partial electric discharges or dielectric breakdown, a process intricately linked to charge migration and storage [22]. The extraction of permittivity ( $\epsilon$ ) and permeability ( $\mu$ ) from S-parameters is indeed complex, as it depends heavily on the extraction model used. We have now explicitly described the NRW (Nicolson–Ross–Weir) method utilized for the extraction of  $\epsilon$  and  $\mu$  values from the measured S-parameters.

Additionally, we have provided a brief comparison with other methods, such as the NRW (Nicolson–Ross–Weir) method [23] and the Boughriet method [24,25], to highlight the robustness and limitations of our chosen model. The sensitivity of the extracted parameters to the model selection has been discussed, acknowledging that different models could yield varying results. However, the NRW method is widely recognized for its reliability in the microwave frequency range, which justifies its use in this study.

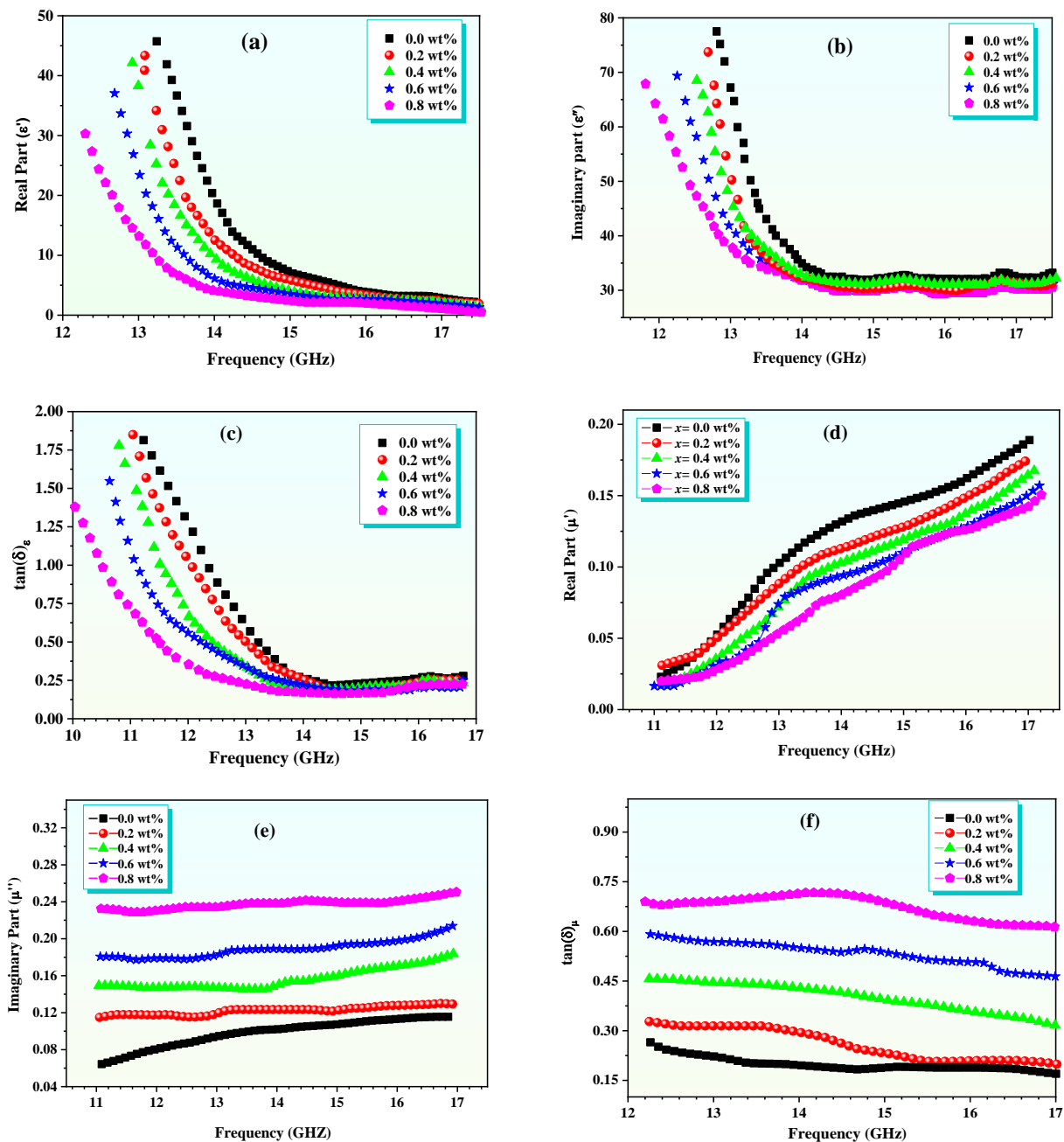


**Figure 4.** Frequency dependence of (a) real part of complex permittivity; (b) imaginary part of complex permittivity; (c)  $\tan(\delta)_\epsilon$  for ZnAl<sub>x</sub>Fe<sub>2-x</sub>O<sub>4</sub>/polypyrrole nanocomposite; (d) real part of complex permeability; (e) imaginary part of complex permeability; (f)  $\tan(\delta)_\mu$  for ZnAl<sub>x</sub>Fe<sub>2-x</sub>O<sub>4</sub>/polypyrrole nanocomposite at  $x = (0.0, 0.2, 0.4, 0.6, 0.8)$  wt.%.

The  $M''$  component delineates two distinct relaxation peaks across different frequency bands. The initial peak, found in the lower frequency domain, underscores the dominant role of interfacial polarization (IP) relaxation phenomena attributed to charge build-up at



the interfaces between the polypyrrole framework and the Zn-Al ferrite particles within the core-shell configurations. The subsequent peak, observed at higher frequencies, is attributed to  $\alpha$ -relaxation, indicative of the local dynamics of polymer chain segments in polypyrrole, particularly dipolar polarization. The intensity of IP peaks surpasses that of the  $\alpha$ -relaxation peaks significantly.

In addition to the NRW method used in this study, other methods, such as the Boughriet method, are also commonly employed for extracting permittivity and permeability from S-parameters. The Boughriet method, while effective in certain contexts, has limitations in terms of its accuracy at higher frequencies and for materials with complex magnetic properties. In contrast, the NRW method is widely recognized for its robustness and reliability, particularly in the microwave frequency range, making it a suitable choice for our study. However, it is important to note that the choice of extraction method can significantly impact the results, and care must be taken to select a method that aligns with the specific characteristics of the material under investigation.

The choice between these methods can significantly influence the results obtained in material characterization. The NRW method's robustness makes it a preferred option for studies involving materials in the microwave frequency range, while the Boughriet method may be more applicable in situations where its specific advantages can be leveraged.

The Cole-Cole plot exhibits a semi-circular trajectory, deviating from the Debye model, followed by a linear increase. This semicircle's radius inversely relates to the composite's electrical conductivity; a larger radius suggests reduced conductivity [26]. The relaxation times ( $\tau_{IP}$ ) for samples with  $x = 0.0$  wt.% and 0.2 wt.% are measured at 12,160.33 ms and 17,054.75 ms, respectively, illustrating the significant influence of  $Al^{3+}$  content on  $\tau_{IP}$  values. The  $\tau_{IP}$  values for Zn-Al ferrite samples are 816 ms and 2289 ms for grain boundary relaxation and 6.19 ms and 41 ms for grain relaxation, respectively. However, the  $\tau_{IP}$  values for  $x = 0.4, 0.6,$  and 0.8 wt.% polypyrrole/Zn-Al ferrite nanocomposites are substantially higher, showing an increase of 7 to 15 times that of the grain boundary relaxation time, highlighting the profound effect of incorporating  $Al^{3+}$  into the matrix.

The impedance spectroscopy has been utilized to explore the electrical characteristics of Zn-Al ferrite/polypyrrole nanocomposites, focusing on the analysis of changes in both the real ( $Z'$ ) and imaginary ( $Z''$ ) components of the impedance across different frequencies. These variations are graphically represented in a Cole-Cole plot, as illustrated in Figure 5, with measurements conducted at room temperature. To comprehend the dynamics between  $Z'$  and  $Z''$  over the entire frequency spectrum, it is essential to consider the behaviors of  $\epsilon'$  and  $\epsilon''$ . Integrating ferrite nanoparticles within the polypyrrole matrix markedly reduces both  $Z'$  and  $Z''$  in the lower frequency domain (11–13 GHz), affecting the polymer matrix's polymerization state and thus disrupting the continuity of its chains. This disruption leads to the emergence of interfacial polarization [24]. Nevertheless, as frequency increases, the significance of interfacial polarization wanes, giving way to the prominence of the charge-hopping mechanism within the Zn-Al ferrite. Between frequencies of 14 and 17 GHz, both  $Z'$  and  $Z''$  demonstrate stability, suggesting that the conductivity of polypyrrole predominates without interference from Zn ferrite, thus establishing a stable conduction pathway. The Cole-Cole plot reveals a semicircle that characterizes the Debye relaxation phenomena, essential for understanding the attenuation of electromagnetic waves.  $Z'$  is indicative of the dissipation component, which accounts for the energy conversion from the input field to thermal energy, subsequently resulting in loss. On the other hand,  $Z''$  represents the impedance's imaginary component, reflecting the non-dissipative segment where the system temporarily stores the energy derived from the field, mimicking an ideal capacitor scenario. The semicircle displayed on the Cole-Cole plot is indicative of various Debye relaxation processes arising due to the interfacial polarization between the Zn-Al ferrite nanoparticles and the conductive polypyrrole matrix, leading to a textbook example of Debye relaxation. The impedance, or Nyquist diagram, delineates the relationship between  $Z'$  and  $Z''$  across varying frequencies (Figure 5), revealing a steady linear escalation across the full frequency range. This trend suggests a direct relationship between the

increase in the dissipative component's ratio and the impedance, which denotes the non-dissipative component. With an increase in frequency, there is a reduction in the energy loss, implying a decrease in the energy transition from the input field to the thermal reservoir, thereby allowing more energy to be conserved within the system.

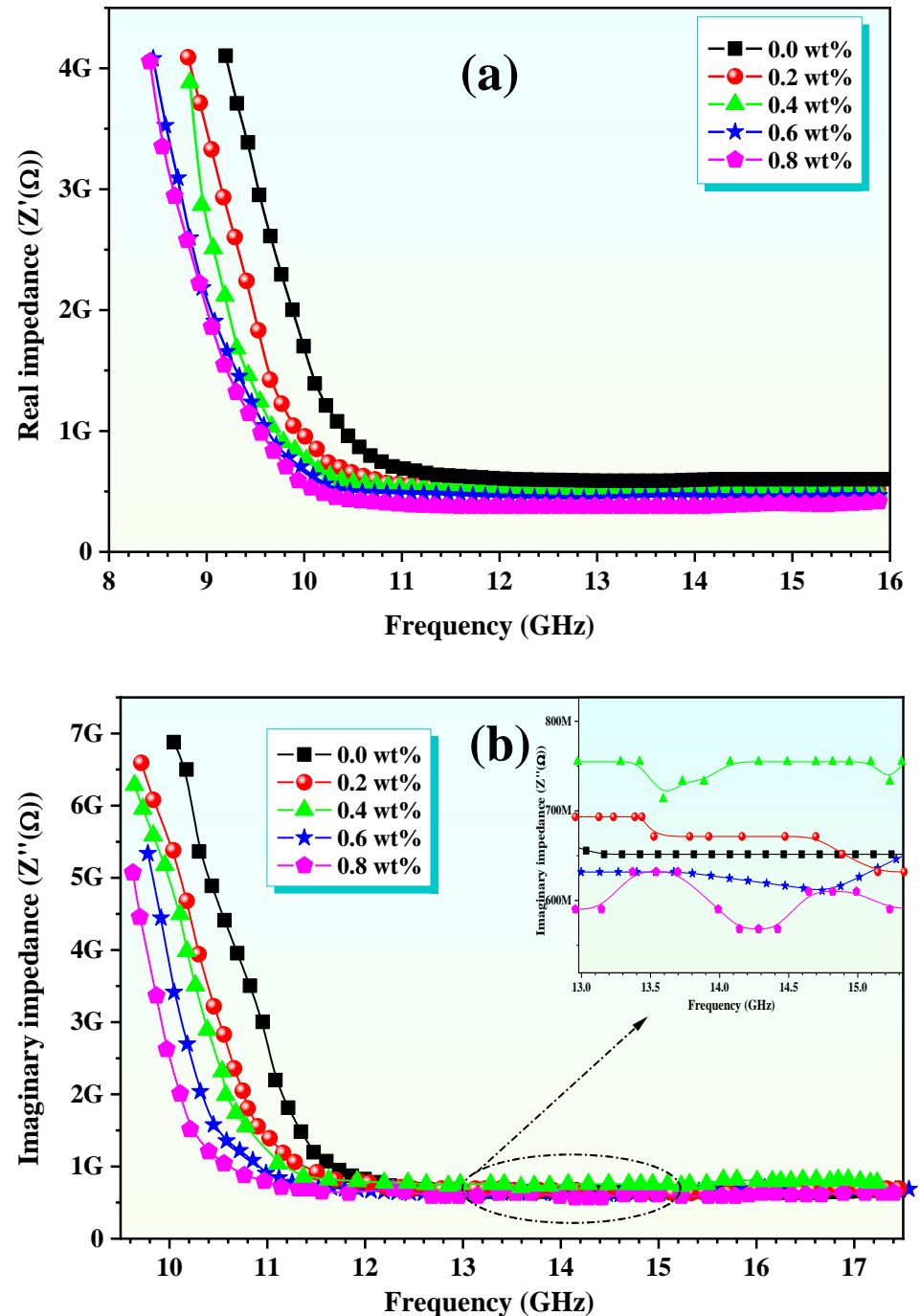


**Figure 5.** Frequency dependence of (a) the real impedance spectra and (b) the imaginary impedance spectra for ZnAl<sub>x</sub>Fe<sub>2-x</sub>O<sub>4</sub>/polypyrrole nanocomposite at  $x = 0.0, 0.2, 0.4, 0.6,$  and  $0.8$  wt%.

The potential applications of Zn-Al/polypyrrole nanocomposites in advancing microwave application efficiency are promising due to their excellent microwave absorption performance. The synergistic effects of magnetic losses and dielectric losses contribute to their efficient electromagnetic wave absorption properties [27]. For instance, ZnFe<sub>2</sub>O<sub>4</sub>/polypyrrole nanocomposites exhibit broadband electromagnetic wave absorp-

tion at 8–18 GHz, with magnetic losses being the main microwave absorption mechanism [28]. Similarly, ZnFe<sub>2</sub>O<sub>4</sub>/SiO<sub>2</sub>/polypyrrole nanocomposites show efficient electromagnetic wave absorption properties in the K and Ka band regions, with magnetic losses and dielectric losses being the primary microwave absorption mechanisms [29]. In addition, the nanocomposites of polypyrrole with Zn-Al-ferrite exhibit a core-shell structure, and the possible bonding effect between metal cations and PPy results in a decrease in conductivity [30]. Microwave measurements are essential for evaluating the electromagnetic interference (EMI) shielding effectiveness (SE) of materials. The SE refers to the ability of a shielding material to attenuate or reduce the propagation of electromagnetic waves. It quantifies the level of attenuation provided by the shielding material and is expressed using Equations (1) and (2):

$$SE(dB) = -10 \log\left(\frac{P_t}{P_i}\right) \tag{4}$$

$$SE_T = SE_R + SE_A + SE_M \tag{5}$$

where  $P_i$  represents the power of the incident electromagnetic wave, and  $P_t$  represents the power of the transmitted electromagnetic wave [31–33]. The total effectiveness of the electromagnetic shielding is being measured, by comparing the power of the electromagnetic waves before they encounter the shielding (the incident power,  $P_i$ ) versus the power of the waves that are able to transmit through the shielding (the transmitted power,  $P_t$ ). For a shielding material, the total shielding effectiveness is the sum of the contribution due to reflection ( $SE_R$ ), absorption ( $SE_A$ ), and multiple reflections ( $SE_M$ ). From the scattering parameters  $S_{11}$  and  $S_{21}$  of a vector network analyzer (measured by waveguide transmission line technique), the reflection coefficient (R) and transmission coefficient (T) can be obtained as  $R = |S_{11}|^2$  and  $T = |S_{21}|^2$ . Using the parameters R and T, the absorption coefficient (A) can be evaluated as  $A + R + T = 1$  [34,35]. With negligible multiple reflections between both interfaces of the material, the relative intensity of the effectively incident EM wave is based on the factor  $(1 - R)$ , and the effective absorption can be expressed as  $A_{eff} = (1 - R - T)/(1 - R)$ . The reflection and effective absorption can be expressed in decibels as  $SE_R$  and  $SE_A$  [36–41]:

$$SE_R = 10 \log(1 - R) \tag{6}$$

$$SE_A = 10 \log\left(1 - A_{eff}\right) = 10 \log\left(\frac{T}{1 - R}\right) \tag{7}$$

When negligible multiple reflections occur between the interfaces of the material, the relative intensity of the effectively incident electromagnetic wave can be estimated using the factor  $(1 - R)$ . This factor determines the effective absorption of the material (Figure 6).

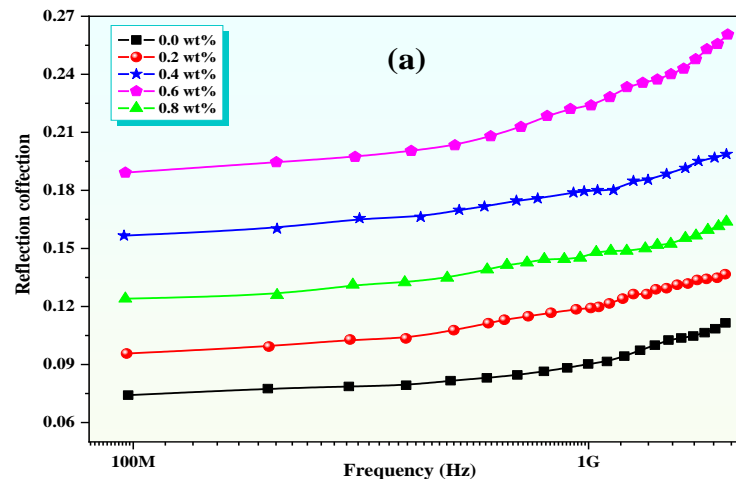
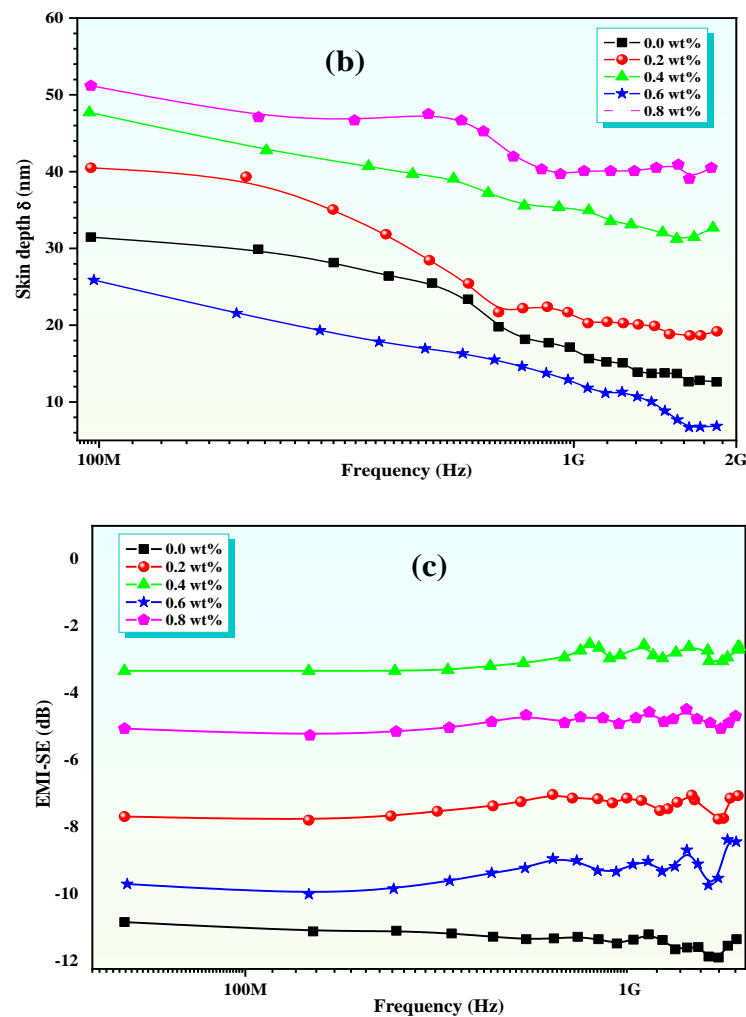


Figure 6. Cont.



**Figure 6.** (a) Reflection coefficient, (b) skin depth, and (c) EMI-SE as a function of frequency for ZnAl<sub>x</sub>Fe<sub>2-x</sub>O<sub>4</sub>/polypyrrole nanocomposite at  $x = 0.0, 0.2, 0.4, 0.6,$  and  $0.8$  wt.%.

## 5. Conclusions

This study presents the successful synthesis and comprehensive characterization of ZnAl<sub>x</sub>Fe<sub>2-x</sub>O<sub>4</sub>/polypyrrole nanocomposites with varying Al content ( $x = 0.0, 0.2, 0.4, 0.6, 0.8$  wt.%). The addition of Al led to significant changes in both structural and magnetic properties, notably reducing the crystal size from 31 nm to 19.6 nm and decreasing the saturation magnetization ( $M_s$ ) from 75 emu/g to 36 emu/g. The core-shell morphology observed in TEM analysis significantly influenced the dielectric behavior, with both real ( $\epsilon'$ ) and imaginary ( $\epsilon''$ ) dielectric constants decreasing as the frequency increased.

The dielectric properties, coupled with the results from impedance spectroscopy, underscore the role of interface polarization, with the relaxation time being notably affected by the Al content. The stability of both  $Z'$  and  $Z''$  within the 14–17 GHz frequency range suggests that the conductivity of polypyrrole predominates without interference from the Zn ferrite, making these nanocomposites particularly promising for microwave absorption applications. Furthermore, the electromagnetic parameters,  $\epsilon$  and  $\mu$ , extracted using the Nicolson–Ross–Weir method, confirmed the material's potential for advanced microwave technologies. The combination of enhanced magnetic–dielectric characteristics points to Zn–Al ferrite/polypyrrole nanocomposites as viable candidates for applications in telecommunications, electromagnetic interference shielding, and other microwave-related technologies.

The Zn–Al ferrite/polypyrrole nanocomposite presents a promising material with enhanced magnetic and dielectric properties compared to previously studied materials.

Its unique combination of properties makes it suitable for a wide range of applications, including magnetic data storage, microwave devices, and energy storage devices.

**Author Contributions:** Conceptualization, methodology, and validation, H.F.K.; resources, M.E.-B.; writing—original draft preparation, S.G.E. and H.F.K.; writing—review and editing, H.F.K. and S.G.E.; visualization, S.G.E.; supervision, M.E.-B.; investigation, resources, funding acquisition, N.F.A.-H. All authors have read and agreed to the published version of the manuscript.

**Funding:** This research received no external funding.

**Institutional Review Board Statement:** We choose to exclude this statement because the study did not require ethical approval.

**Data Availability Statement:** The authors confirm that the data supporting the findings of this study are available within the article.

**Acknowledgments:** The researchers would like to thank the Deanship of Graduate Studies and Scientific Research at Qassim University for financial support (QU-APC-2024-9/1).

**Conflicts of Interest:** The authors declare no conflict of interest.

## References

1. Elmahaishi, M.F.; Azis, R.S.; Ismail, I.; Muhammad, F.D. A review on electromagnetic microwave absorption properties: Their materials and performance. *J. Mater. Res. Technol.* **2022**, *20*, 2188–2220. [[CrossRef](#)]
2. Klimov, A.S.; Bakeev, I.Y.; Dolgova, A.V.; Kazakov, A.V.; Korablev, N.S.; Zenin, A.A. Features of Electron Beam Processing of Mn-Zn Ferrites in the Fore-Vacuum Pressure Range in Continuous and Pulse Modes. *Coatings* **2023**, *13*, 1766. [[CrossRef](#)]
3. Vissurkhanova, Y.A.; Ivanova, N.M.; Soboleva, Y.A.; Muldakhmetov, Z.M.; Abulyaissova, L.K.; Minaev, B.F. Fe-Cu composites preparation using Cu-Zn ferrite and their electrocatalytic application. *Mater. Lett.* **2023**, *333*, 133521. [[CrossRef](#)]
4. Joulaei, M.; Hedayati, K.; Ghanbari, D. Investigation of magnetic, mechanical and flame retardant properties of polymeric nanocomposites: Green synthesis of MgFe<sub>2</sub>O<sub>4</sub> by lime and orange extracts. *Compos. Part B Eng.* **2019**, *176*, 107345. [[CrossRef](#)]
5. Hajlaoui, M.E.; Dhahri, R.; Hnainia, N.; Benchaabane, A.; Dhahri, E.; Khirouni, K. Conductivity and giant permittivity study of Zn<sub>0.5</sub>Ni<sub>0.5</sub>Fe<sub>2</sub>O<sub>4</sub> spinel ferrite as a function of frequency and temperature. *RSC Adv.* **2019**, *9*, 32395–32402. [[CrossRef](#)]
6. Ahmad, M.; Amin, K.; Rehman, A.U.; Wahab, A.; Wabaidur, S.M. Detailed investigation of Mn-substituted Zn ferrites for microwave applications up to 6 GHz. *Mater. Sci. Technol.* **2024**, *40*, 479–492. [[CrossRef](#)]
7. Ajeel, K.I.; Kareem, Q.S. Synthesis and Characteristics of Polyaniline (PANI) Filled by Graphene (PANI/GR) nano-Films. *J. Phys. Conf. Ser.* **2019**, *1234*, 012020. [[CrossRef](#)]
8. Rybicki, T.; Stempien, Z.; Karbownik, I. EMI Shielding and Absorption of Electroconductive Textiles with PANI and PPy Conductive Polymers and Numerical Model Approach. *Energies* **2021**, *14*, 7746. [[CrossRef](#)]
9. Mamatha, G.M.; Pradipkumar Dixit RHari Krishna Girish Kumar, S. Polymer based composites for electromagnetic interference (EMI) shielding: The role of magnetic fillers in effective attenuation of microwaves, a review. *Hybrid Adv.* **2024**, *6*, 100200.
10. Khalil, H.F.; Malidarreh, R.B.; Alabsy, M.T.; Hassan, A.M.; El-Khatib, A.M.; Issa, S.A.; Zakaly, H.M. Structural, Morphological, and  $\gamma$ -ray Attenuation properties of m-type hexaferrite BaFe<sub>12</sub>O<sub>19</sub> doped with V<sub>2</sub>O<sub>5</sub>, Ce<sub>2</sub>O<sub>3</sub> and Bi<sub>2</sub>O<sub>3</sub> for Radiation Shielding applications. *Ceram. Int.* **2024**, *50*, 33771–33780. [[CrossRef](#)]
11. Devi, R.; Patra, J.; Tapadia, K.; Chang, J.-K.; Maharana, T. Arrangement of ZnFe<sub>2</sub>O<sub>4</sub>@PPy nanoparticles on carbon cloth for highly efficient symmetric supercapacitor. *J. Taiwan Inst. Chem. Eng.* **2022**, *138*, 104474. [[CrossRef](#)]
12. Elahi, A.; Shakoor, A.; Irfan, M.; Mahmood, K.; Niaz, N.A.; Awan, M.S.; Bashir, T. Polypyrrole and its nanocomposites with Zn<sub>0.5</sub>Ni<sub>0.4</sub>Cr<sub>0.1</sub>Fe<sub>2</sub>O<sub>4</sub> ferrite: Preparation and electromagnetic properties. *J. Mater. Sci. Mater. Electron.* **2016**, *27*, 6964–6973. [[CrossRef](#)]
13. Khan, M.Z.; Gul, I.H.; Baig, M.M.; Khan, A.N. Comprehensive study on structural, electrical, magnetic and photocatalytic degradation properties of Al<sup>3+</sup> ions substituted nickel ferrites nanoparticles. *J. Alloys Compd.* **2020**, *848*, 155795. [[CrossRef](#)]
14. Carrara, S. Towards New Efficient Nanostructured Hybrid Materials for ECL Applications. Ph.D. Thesis, Université de Strasbourg, Strasbourg, France, 2017.
15. Khafagy, R.M. Synthesis, characterization, magnetic and electrical properties of the novel conductive and magnetic Polyaniline/MgFe<sub>2</sub>O<sub>4</sub> nanocomposite having the core-shell structure. *J. Alloys Compd.* **2021**, *509*, 9849–9857. [[CrossRef](#)]
16. Ben Farhat, L.; Ben Ahmed, S.; Ezzine, S.; Amami, M. Particle size dependent structural, magnetic and electrical properties of Cr-doped lead-free multiferroic AlFeO<sub>3</sub> prepared by co-precipitation and solid state method. *Mater. Chem. Phys.* **2020**, *255*, 123631. [[CrossRef](#)]
17. Srinivasulu, T.; Saritha, K.; Reddy, K.R. Synthesis and characterization of Fe-doped ZnO thin films deposited by chemical spray pyrolysis. *Mod. Electron. Mater.* **2017**, *3*, 76–85. [[CrossRef](#)]
18. Nigam, A.; Pawar, S. Structural, magnetic, and antimicrobial properties of zinc doped magnesium ferrite for drug delivery applications. *Ceram. Int.* **2020**, *46*, 4058–4064. [[CrossRef](#)]

19. Soin, N. *Magnetic Nanoparticles—Piezoelectric Polymer Nanocomposites for Energy Harvesting, Magnetic Nanostructured Materials*; Elsevier: Amsterdam, The Netherlands, 2018; pp. 295–322.
20. Wan, C.; Bowen, C.R. Multiscale-structuring of polyvinylidene fluoride for energy harvesting: The impact of molecular-, micro- and macro-structure. *J. Mater. Chem. A* **2017**, *5*, 3091–3128. [[CrossRef](#)]
21. Wu, Y.; Hsu, S.L.; Honeker, C.; Bravet, D.J.; Williams, D.S. The Role of Surface Charge of Nucleation Agents on the Crystallization Behavior of Poly(vinylidene fluoride). *J. Phys. Chem. B* **2012**, *116*, 7379–7388. [[CrossRef](#)]
22. Ma, Y.; Tong, W.; Wang, W.; An, Q.; Zhang, Y. Montmorillonite/PVDF-HFP-based energy conversion and storage films with enhanced piezoelectric and dielectric properties. *Compos. Sci. Technol.* **2018**, *168*, 397–403. [[CrossRef](#)]
23. Zhang, S.; Tong, W.; Wang, J.; Wang, W.; Wang, Z.; Zhang, Y. Modified sepiolite/PVDF-HFP composite film with enhanced piezoelectric and dielectric properties. *J. Appl. Polym. Sci.* **2019**, *137*, 48412. [[CrossRef](#)]
24. Kusuma, D.Y.; Nguyen, C.A.; Lee, P.S. Enhanced ferroelectric switching characteristics of P(VDF-TrFE) for organic memory devices. *J. Phys. Chem. B* **2010**, *114*, 13289–13293. [[CrossRef](#)] [[PubMed](#)]
25. Lei, D.; Hu, N.; Wu, L.; Alamusi, N.; Ning, H.; Wang, Y.; Jin, Z.; Liu, Y. Improvement of the piezoelectricity of PVDF-HFP by CoFe<sub>2</sub>O<sub>4</sub> nanoparticles. *Nano Mater. Sci.* **2023**, *6*, 201–210. [[CrossRef](#)]
26. Durgaprasad, P.; Hemalatha, J. Magnetolectric investigations on poly (vinylidene fluoride)/CoFe<sub>2</sub>O<sub>4</sub> flexible electrospun membranes. *J. Magn. Magn. Mater.* **2018**, *448*, 94–99. [[CrossRef](#)]
27. Rothwell, E.J.; Frasch, J.L.; Ellison, S.M.; Chahal, P.; Ouedraogo, R.O. Analysis of the Nicolson-Ross-Weir Method for Characterizing the Electromagnetic Properties of Engineered Materials. *Prog. Electromagn. Res.* **2016**, *157*, 31–47. [[CrossRef](#)]
28. Costa, F.; Borgese, M.; Degiorgi, M.; Monorchio, A. Electromagnetic Characterisation of Materials by Using Transmission/Reflection (T/R) Devices. *Electronics* **2017**, *6*, 95. [[CrossRef](#)]
29. Barroso, J.J.; de Paula, A.L. Retrieval of Permittivity and Permeability of Homogeneous Materials from Scattering Parameters. *J. Electromagn. Waves Appl.* **2010**, *24*, 1563–1574. [[CrossRef](#)]
30. Indrakanti, R.; Brahmaji Rao, V.; Udaya Kiran, C. Optical parameters of gallium nitride doped ferrite–polypyrrole nanocomposites. *J. Mater. Sci. Mater. Electron.* **2020**, *31*, 3238–3244. [[CrossRef](#)]
31. Martins, P.; Costa, C.M.; Lanceros-Mendez, S. Nucleation of electroactive  $\beta$ -phase poly(vinylidene fluoride) with CoFe<sub>2</sub>O<sub>4</sub> and NiFe<sub>2</sub>O<sub>4</sub> nanofillers: A new method for the preparation of multiferroic nanocomposites. *Appl. Phys. A* **2010**, *103*, 233–237. [[CrossRef](#)]
32. Manohar, A.; Geleta, D.D.; Krishnamoorthi, C.; Lee, J. Synthesis, characterization and magnetic hyperthermia properties of nearly monodisperse CoFe<sub>2</sub>O<sub>4</sub> nanoparticles. *Ceram. Int.* **2020**, *46*, 28035–28041. [[CrossRef](#)]
33. Kolhar, P.; Sannakki, B. Investigation of the electrical properties of synthesised polyaniline-magnesium ferrite composites. *Mater. Today Proc.* **2023**, *422*, 2214–7853. [[CrossRef](#)]
34. Ge, Y.; Li, C.; Waterhouse, G.I.N.; Zhang, Z.; Yu, L. ZnFe<sub>2</sub>O<sub>4</sub>@SiO<sub>2</sub>@Polypyrrole nanocomposites with efficient electromagnetic wave absorption properties in the K and Ka band regions. *Ceram. Int.* **2021**, *47*, 1728–1739. [[CrossRef](#)]
35. Li, F.; Zhuang, L.; Zhan, W.; Zhou, M.; Sui, G.; Zho, A.; Bai, G.; Xia, W.; Yang, X. Desirable micro-wave absorption performance of ZnFe<sub>2</sub>O<sub>4</sub>@ZnO@rGO nanocomposites based on controllable permittivity and permeability. *Ceram. Int.* **2020**, *46*, 21744–21751. [[CrossRef](#)]
36. Dong, S.; Zhang, X.; Li, X.; Chen, J.; Hu, P.; Han, J. SiC whiskers-reduced graphene oxide composites decorated with MnO nanoparticles for tunable microwave absorption. *Chem. Eng. J.* **2020**, *392*, 123817. [[CrossRef](#)]
37. Liu, P.-J.; Yao, Z.-J.; Ng, V.M.H.; Zhou, J.-T.; Yang, Z.-H.; Kong, L.-B. Enhanced Microwave Absorption Properties of Double-Layer Absorbers Based on Spherical NiO and Co<sub>0.2</sub>Ni<sub>0.4</sub>Zn<sub>0.4</sub>Fe<sub>2</sub>O<sub>4</sub> Ferrite Composites. *Acta Met. Sin.* **2018**, *31*, 171–179. [[CrossRef](#)]
38. Choi, M.; Lee, S.; Kim, J. Clustering effect on the frequency-dependent magnetic properties of Fe–Co micro hollow fiber composites. *IEEE Trans. Magn.* **2017**, *53*, 1–5. [[CrossRef](#)]
39. Wang, J.-H.; Wu, R.-Z.; Feng, J.; Zhang, J.-H.; Hou, L.-G.; Liu, M.-D. Recent advances of electromagnetic interference shielding Mg matrix materials and their processings: A review. *Trans. Nonferrous Met. Soc. China* **2022**, *32*, 1385–1404. [[CrossRef](#)]
40. Wang, J.; Li, Y.; Wu, R.; Xu, L.; Zhang, Z.; Feng, J.; Zhang, J.; Hou, L.; Jiao, Y. X-band shielding properties of Mg–9Li matrix composite containing Ni<sub>0.4</sub>Zn<sub>0.4</sub>Co<sub>0.2</sub>Fe<sub>2</sub>O<sub>4</sub> fabricated by multi-layer composite rolling. *J. Alloys Compd.* **2020**, *843*, 156053. [[CrossRef](#)]
41. Kruželák, J.; Kvasničáková, A.; Hložeková, K.; Hudec, I. Progress in polymers and polymer composites used as efficient materials for EMI shielding. *Nanoscale Adv.* **2021**, *3*, 123–172. [[CrossRef](#)]

**Disclaimer/Publisher’s Note:** The statements, opinions and data contained in all publications are solely those of the individual author(s) and contributor(s) and not of MDPI and/or the editor(s). MDPI and/or the editor(s) disclaim responsibility for any injury to people or property resulting from any ideas, methods, instructions or products referred to in the content.